This paper is published as part of a *Dalton Transactions* themed issue on:

Thermoelectric Materials

Guest Editor Andrei Shevelkov
Moscow State University, Russia

Published in issue 4, 2010 of *Dalton Transactions*

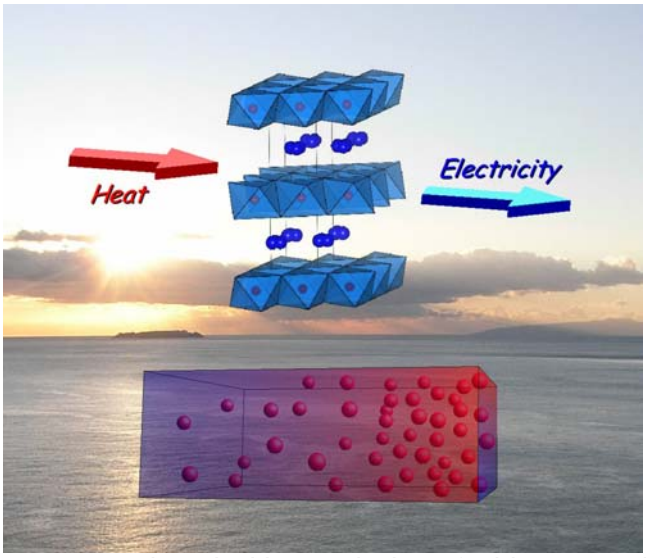

Image reproduced with permission of Ichiro Terasaki

Articles published in this issue include:

PERSPECTIVES:

Thermoelectric clathrates of type I
Mogens Christensen, Simon Johnsen and Bo Brummerstedt Iversen
Dalton Trans., 2010, DOI: 10.1039/b916400f

Wet chemical synthesis and thermoelectric properties of V-VI one- and two-dimensional nanostructures
Genqiang Zhang, Qingxuan Yu and Xiaoguang Li
Dalton Trans., 2010, DOI: 10.1039/b913462j

HOT ARTICLES:

Novel thermoelectric properties of complex transition-metal oxides
Ichiro Terasaki, Manabu Iwakawa, Tomohito Nakano, Akira Tsukuda and Wataru Kobayashi**,**
Dalton Trans., 2010, DOI: 10.1039/b914661j

Effect of Zn doping on improving crystal quality and thermoelectric properties of borosilicides
Takao Mori, David Berthebaud, Toshiyuki Nishimura, Akiko Nomura, Toetsu Shishido and Kazuo Nakajima, *Dalton Trans.,* 2010, DOI: 10.1039/b916028k

Visit the *Dalton Transactions* website for more cutting-edge inorganic and organometallic research
www.rsc.org/dalton

Electronic structure and transport in thermoelectric compounds AZn_2Sb_2 (A = Sr, Ca, Yb, Eu)

Eric S. Toberer,[a] Andrew F. May,[b] Brent C. Melot,[c] Espen Flage-Larsen[d] and G. Jeffrey Snyder*[a]

Received 15th July 2009, Accepted 16th September 2009
First published as an Advance Article on the web 23rd October 2009
DOI: 10.1039/b914172c

The AZn_2Sb_2 ($P\bar{3}m1$, A = Ca, Sr, Eu, Yb) class of Zintl compounds has shown high thermoelectric efficiency ($zT \sim 1$) and is an appealing system for the development of Zintl structure–property relationships. High temperature transport measurements have previously been conducted for all known compositions except for $SrZn_2Sb_2$; here we characterize polycrystalline $SrZn_2Sb_2$ to 723 K and review the transport behavior of the other compounds in this class. Consistent with the known AZn_2Sb_2 compounds, $SrZn_2Sb_2$ is found to be a hole-doped semiconductor with a thermal band gap ~ 0.27 eV. The Seebeck coefficients of the AZn_2Sb_2 compounds are found to be described by similar effective mass ($m^* \sim 0.6\ m_e$). Electronic structure calculations reveal similar m^* is due to antimony p states at the valence band edge which are largely unaffected by the choice of A-site species. However, the choice of A-site element has a dramatic effect on the hole mobility, with the room temperature mobility of the rare earth-based compositions approximately double that found for Ca and Sr on the A site. This difference in mobility is examined in the context of electronic structure calculations.

Introduction

The need for sustainable energy sources has led to a renewed interest in thermoelectric materials for power generation. Thermoelectric generators can utilize waste heat sources or be employed in co-generation systems. Widespread application of thermoelectric generators is contingent upon the discovery of materials which have higher thermoelectric efficiencies and are more environmentally benign and inexpensive than the current state-of-the-art materials.[1] The efficiency of a thermoelectric generator is determined by the Carnot efficiency ($\eta_c = \Delta T/T_{hot}$) and the thermoelectric figure of merit, zT ($zT = \alpha^2 T/\rho k$). Thus a good thermoelectric material couples a large Seebeck coefficient (α) with low electrical resistivity (ρ) and thermal conductivity (κ). The favorable combination of all three properties in a material is unusual and most frequently is found in heavily doped semiconductors with carrier concentrations ranging from 10^{19}–10^{20} carriers/cm^3. Binary semiconductors such as Bi_2Te_3 and PbTe continue to represent the state-of-the-art in commercially available thermoelectric devices with peak $zT \sim 1$.

In the search for high performance bulk materials, Zintl phases have been particularly rewarding. Zintl phases are composed of electropositive cations (alkali, alkaline-earth or rare earth) that donate electrons to anions, which may form covalent bonds to satisfy valence.[2] Zintl compounds such as $CeCoFe_3Sb_{12}$, $Yb_{14}MnSb_{11}$, and $Ba_8Ga_{16}Ge_{30}$ have all demonstrated high thermoelectric efficiency ($zT \geq 1$), and many others have shown promising preliminary results.[3-6] In Zintl compounds, complex crystal structures often lead to low lattice thermal conductivity while covalent bonding maintains reasonable carrier mobility. However, unifying relationships between crystal structure and charge carrier/phonon transport remain in their infancy. This is especially difficult in Zintl compounds due to their complexity.

One class of Zintl compounds which has shown promising thermoelectric efficiency is based on the $CaAl_2Si_2$ structure type, shown in Fig. 1 ($P\bar{3}m1$). Using the Zintl formalism, we can describe the structure as trigonal monolayers of A^{2+} cations in the a–b plane separating $(Zn_2Sb_2)^{2-}$ covalently bound slabs. The anionic slabs can be viewed as two puckered graphitic Sb–Zn layers which have been brought into contact. Burdett and Miller have described the bonding characteristics of $CaAl_2Si_2$-type compounds in great detail.[7] High zT has been reported for $EuZn_2Sb_2$ (0.9 at 700 K[8])

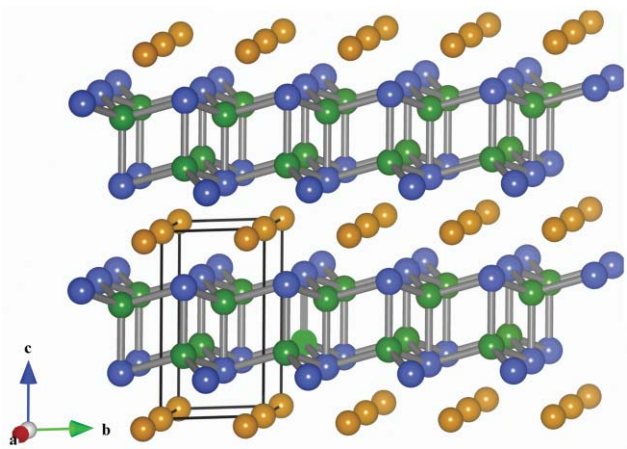

Fig. 1 $SrZn_2Sb_2$ ($P\bar{3}m1$) structure consists of a trigonal monolayer of Sr (orange) separated by covalently bound slabs of Zn–Sb (Zn – green, Sb – blue).

[a]*Materials Science, California Institute of Technology, 1200 E. California Blvd., Pasadena, California 91125, USA. E-mail: jsnyder@caltech.edu*
[b]*Chemical Engineering, California Institute of Technology, 1200E. California Blvd., Pasadena, California, 91125, USA*
[c]*Materials Department and Materials Research Laboratory, University of California, Santa Barbara, CA 93106, USA*
[d]*Department of Physics, University of Oslo, P.O. Box 1048 Blindern, N-0316, Oslo, Norway*

and $YbZn_{2-x}Cd_xSb_2$ (1.2 at 700 K[9]). Likewise, solid solutions of $Ca_xYb_{1-x}Zn_2Sb_2$ ($0 \le x \le 1$)[10] and $YbZn_{2-x}Mn_xSb_2$ ($0 \le x \le 0.4$)[11] have shown moderate zT (~0.5 at 700 K). Moving down Group II, $BaZn_2Sb_2$ ($I4/mmm$) adopts a channel structure and a peak zT of 0.3 has been reported.[12]

Here we explore the final known $P\text{-}3m1$ AZn_2Sb_2 compound, $SrZn_2Sb_2$,[13] and develop general relationships for these materials through a combination of calculations and classical transport theory.

Table 1 Transport properties of AZn_2Sb_2 at 300 K. Shown are the Seebeck coefficient α, the electrical resistivity ρ, the mobility μ, the free carrier concentration n and the total thermal conductivity κ. Data for the Ca, Yb and Eu compounds are from respective references

	Sr	Ca [10]	Yb [10]	Eu [8]
α [μV/K]	159	120	48	120
ρ [mΩ cm]	4.5	2.37	0.32	0.88
μ [cm^2/Vs]	95	83	130	257
n [10^{19} cm^{-3}]	1.5	3.1	15	2.77
κ [W/mK]	2.05	2.6	4.25	2.5

Sample preparation and choice of methods

Synthesis

$SrZn_2Sb_2$ was prepared by direct reaction of the elements in boron nitride crucibles within fused-silica ampoules sealed under dynamic vacuum (10^{-5} torr). The reactants were melted by heating to 1223 K over 15 h followed by an isothermal hold for 30 minutes. The ampoules were cooled to 823 K over 2 h, followed by an 8 h anneal at 823 K. To provide homogeneous fine grain powders for sintering, mechanical alloying was performed under argon in a SPEX Mixer/Miller 8000 series mill. Hot pressing of the resulting powder was performed under argon at 823 K for 1 h.

Characterization

Following hot pressing, the resulting ingots were sliced into disks (1 mm thick, 12 mm diameter) and the high temperature transport properties were characterized to 723 K under a dynamic vacuum. Electrical resistivity was determined using the van der Pauw technique and the Hall coefficient was measured with a 2 T field and pressure-assisted contacts.[14] The Seebeck coefficient was measured with a constant 10 K temperature gradient across the sample and Chromel-Nb thermocouples. A Netzsch LFA 457 was used to measure thermal diffusivity and the heat capacity was estimated using the method of Dulong–Petit. Powder XRD patterns were measured on a Philips XPERT MPD diffractometer operated at 45 kV and 40 mA and subject to Rietveld refinement using the XND Rietveld code.[15]

Electronic structure calculations

Density functional theory (DFT) calculations of the electronic structure were performed using the Vienna *Ab-initio* Simulation Package (VASP)[16,17] package. The highly efficient projector augmented-wave (PAW) method[18] was used together with the generalized gradient approximation Perdew–Burke–Ernzerhof[19] (GGA-PBE) exchange–correlation functional. All 4*f* states of Yb as well as the 4*s* states of Zn were included and the calculations were evaluated at the experimental lattice parameters shown in Table 2 (values from ref. 10 and this work).

A plane-wave energy cutoff of 500 eV and a $12 \times 12 \times 8$ Γ-centered k-point mesh was used to sample the Brillouin zone. The tetrahedron method with Blöchl correction[20] was used for Brillioun zone integrations in the density of state calculations, while for the band structure calculations a Gaussian broadening of 0.05 eV was used.

It is well established that systems with partially filled and sometimes even closed d and f states are not well described by standard DFT methods because of the improper treatment of the exchange–correlation functional. As an alternative we use the GGA+U formalism of the rotationally invariant approach of Liechtenstein *et al.*[21] GGA+U includes a Hubbard U parameter to account for the on-site Coulomb interaction and a J parameter to account for exchange. A U of 5.3 eV and a J of 0 eV were selected for Yb in order to agree with previously published results based upon photoemission studies.[22,23]

A Hubbard U was also applied to the Zn d states in order to obtain a semi-conducting ground state. This was needed to obtain reasonable agreement between the electronic transport measurements and calculations. The U term has the effect of moving the d states closer to the atomic core, thus generating a small Coulombic repulsion with the s states. The spherical symmetry of the s states results in a symmetric delocalization of the orbitals which pushes them slightly higher in energy. Due to the presence of s at the conduction band edge and their absence in the top valence region, this opens a gap. Given that the Zn d manifolds sit deep in the valence region (approx. 7 eV before the addition of the U) this should have little effect on the features of the band structure other than for the s states around the gap (for minor changes in U). A value of 10 eV was needed to open a small gap in the $SrZn_2Sb_2$ compound. The same value of U was then used for the Ca and Yb compounds.

Even though the spin–orbit coupling of the Zn d states might be of importance to the transport properties, the applied U parameter is artificial (to open the gap). It is also expected that the spin–orbit

Table 2 Structural properties of AZn_2Sb_2. Lattice parameters a and c, Wyckoff positions, ionic radius and Pauling electronegativity of the A sites are given.[13] In addition the puckering angle between Zn and Sb and their respective bond distances are shown (bonds along the c-axis, 'a–b' plane). Wyckoff positions not reported for $EuZn_2Sb_2$; $YbZn_2Sb_2$ positions are determined from laboratory X-ray diffraction

A	a (Å)	c (Å)	Zn position	Sb position	A radius (Å)	A-site Pauling χ	puckering angle (°)	Zn–Sb bond distances (Å)
Sr	4.500	7.716	0.6311	0.2688	1.18	0.95	16.56	2.796, 2.7105
Ca	4.441	7.464	0.6307	0.2571	1.00	1.0	18.09	2.789, 2.6973
Yb	4.446	7.426	0.6313	0.2418	1.02	1.11	20.16	2.892, 2.7344
Eu	4.489	7.6009	—	—	1.17	1.20	—	—

correction is rather small (free atom split of ~0.1 eV). To keep consistency, spin–orbit corrections for the Yb *f* states are not calculated, even though they are thought to be of more significance (free atom split of ~1.2 eV).

First principle electronic transport calculations

The electronic transport properties were calculated using the Boltzmann transport equations within the time relaxation approximation.[24] A momentum matrix perturbation approach was used to calculate the band velocities. Convergence of the Seebeck coefficient as a function of carrier concentration at 300 K was obtained for a Γ-centered 24 × 24 × 12 *k*-point grid that was post-interpolated to a 208 × 208 × 100 *k*-point grid.

Results and discussion

Experimental properties

The direct reaction of the elements followed by hot pressing resulted in dense (>95% theoretical density), homogeneous ingots of $SrZn_2Sb_2$. Rietveld refinement of the resulting $SrZn_2Sb_2$ (Fig. 2) agrees with the previously published structure,[13] and the structure parameters are given in Table 2. Consistent with prior work on AZn_2Sb_2, an impurity of the semiconductor ZnSb (approx. 6 vol%, average grain size ~5 μm) was also observed. Backscattering scanning electron microscopy and energy-dispersive spectroscopy (EDS) support these diffraction results.

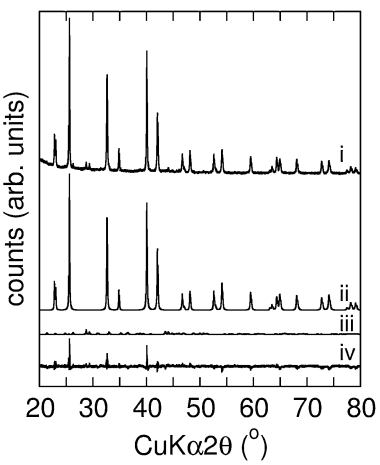

Fig. 2 (i) X-ray diffraction pattern, Rietveld refinement to the (ii) $SrZn_2Sb_2$ and (iii) ZnSb phases, and (iv) difference profile (top to bottom).

Electronic transport. To assess the thermoelectric performance of $SrZn_2Sb_2$, measurements of the electrical resistivity, Seebeck coefficient, and thermal diffusivity were conducted from 300 to 723 K. Hall effect measurements were performed to aid in the analysis of these measurements.

Measurement of the Hall coefficient of $SrZn_2Sb_2$ reveals holes are the majority carrier at room temperature ($n_H = 1/R_He$). The unintentionally doped sample has a carrier concentration of 1.5×10^{19} h^+ cm^{-3} at room temperature, which is less than the other AZn_2Sb_2 compounds previously studied (Table 1). The carrier concentration of $SrZn_2Sb_2$ is constant through to ~600 K (Fig. 2a), indicating the domination of extrinsic carriers. At high temperatures, a sharp rise in carrier concentration is observed due to the excitation of minority carriers across the band gap. In this high temperature bipolar regime, a single carrier type description is no longer accurate and the presence of electrons leads to an overestimation of the hole carrier concentration. A similar transition from extrinsic to intrinsic carriers was observed for $CaZn_2Sb_2$, while $YbZn_2Sb_2$ was too heavily doped to observe significant carrier activation within the measurement temperature range.[10]

Previous work on $Ca_xYb_{1-x}Zn_2Sb_2$ noted that while they have nearly identical structures, their carrier concentrations follow trend with electronegativity of the *A* cation.[10] This trend was attributed to the greater tendency of more electronegative Yb to donate fewer electrons and therefore produce holes. The carrier concentration of $SrZn_2Sb_2$ indeed nicely follows and extends the same trend of observed carrier concentration with electronegativity. However, we now believe AZn_2Sb_2 are semiconducting Zintl compounds and partial electron donation is not consistent with this understanding.

In a simple ionic semiconductor, the valence band edge is dominated by anion states. The difference in electronegativity between cations and anions can affect band characteristics such as band mass and energy gap, but does not alter the number of states in the band. More electronegative cations will shift the distribution of electron density (discussed below, Fig 9), leading to more covalent bonding.

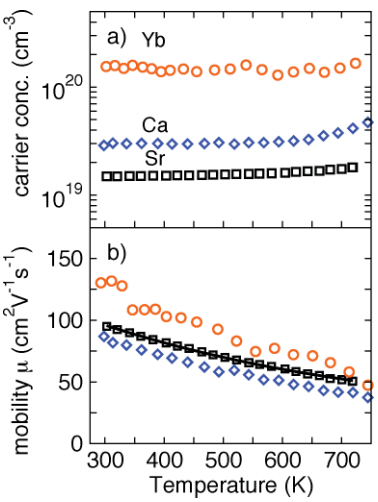

Fig. 3 Hall effect measurements on $SrZn_2Sb_2$ are used to calculate the (a) carrier concentration and (b) mobility to 725 K. The solid line shows a $T^{-1.5}$ fit, as expected for phonon dominated mobility in a lightly doped semiconductor.

In the $Ca_xYb_{1-x}Zn_2Sb_2$ system, hole-doped semiconducting behavior was observed for nominally stoichiometric compositions. If this behavior originates from the band structure, a partially filled valence band would be required, with additional states arising from changes to bonding and/or valency. Such a band structure would likely resemble a semimetal with the Fermi level crossing a number of bands with both *n* and *p*-type character, as seen in $Yb_5Al_2Sb_6$.[25] However, the transport properties (constant carrier concentration with increasing temperature, linearly increasing resistivity and Seebeck coefficient at low temperature and maximum in Seebeck coefficient and resistivity at high temperature) suggests

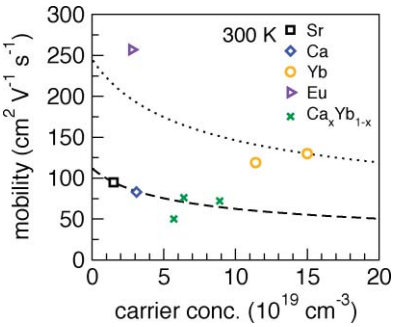

Fig. 4 Room temperature mobility for AZn_2Sb_2 (A = Sr, Ca,[10] Yb,[9,10] Eu[8]), and the $Ca_xYb_{1-x}Zn_2Sb_2$ solid solution.[10] Dashed lines obtained from classical transport equations using $SrZn_2Sb_2$ and $YbZn_2Sb_2$ properties and the assumption of mobility limited by acoustic phonon scattering.

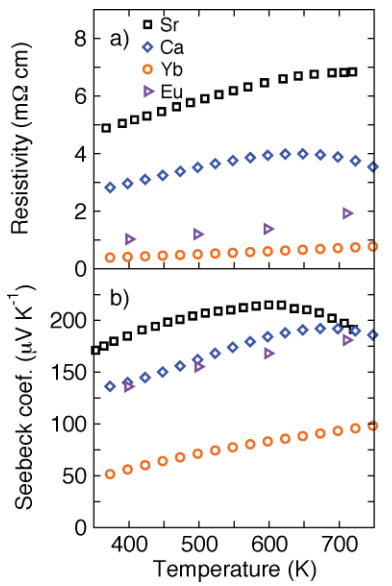

Fig. 5 (a) Electrical resistivity and (b) Seebeck coefficients of AZn_2Sb_2 (A = Sr, Ca, Yb, Eu). Data obtained from references in Fig. 4.

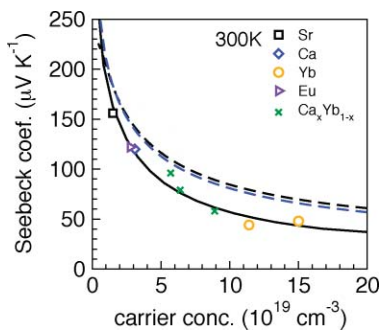

Fig. 6 Room temperature Seebeck coefficients for the AZn_2Sb_2 series and a single parabolic band model using an effective mass of 0.56 m_e (solid line). Dashed lines from $SrZn_2Sb_2$ and $CaZn_2Sb_2$ density functional calculations using the energy independent relaxation time approximation. Data obtained from references in Fig. 4.

AZn_2Sb_2 compounds are simple semiconductors, not semimetals. Furthermore, the simple structure of AZn_2Sb_2 does not promote partial bond formation and the valence states of the constituent atoms are well defined.

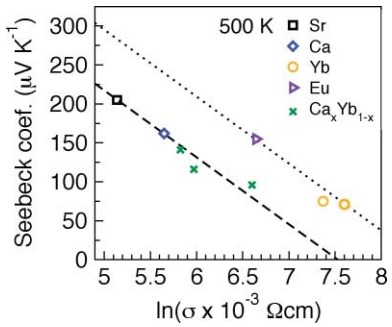

Fig. 7 Increased conductivity is found for A = Yb, Eu compared to A = Ca, Sr at 500 K. The dashed lines show the expected slope (−86 μV/K) for single parabolic band behavior. Data obtained from references in Fig. 4.

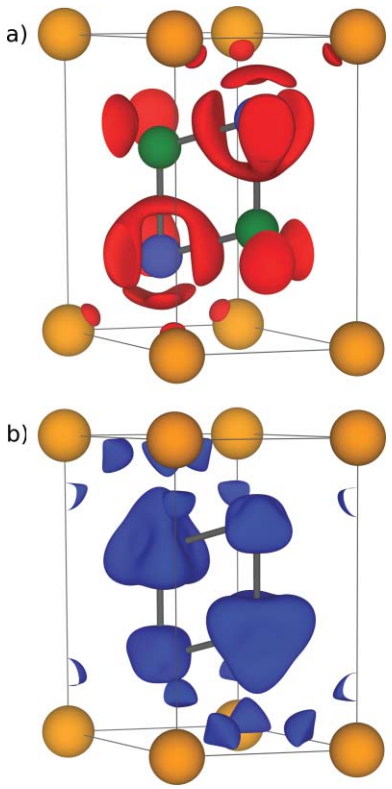

Fig. 8 Electron density difference isosurfaces for $SrZn_2Sb_2$ for regions of (a) charge accumulation (4.1×10^{-3} electrons bohr^{-3} cutoff) and (b) charge depletion (2.5×10^{-3} electrons bohr^{-3} cutoff) reveal bonding from Sb (blue) to both Zn (green) and Sr (orange).

We now believe that the observation of extrinsic carriers is due to A site vacancies. The presence of uncompensated cation vacancies would lead to hole formation ($V''_A + 2h^{\bullet}$). A-site vacancies are consistent with the observation of ZnSb as a secondary phase in these samples, with the majority phase the cation deficient ($A_{1-y}Zn_2Sb_2$) at the phase boundary edge with ZnSb.

The observed trend between carrier concentration and A-site electronegativity appears to be consistent with this vacancy hypothesis. Increasing the electronegativity difference between cations and anions should increase the energy required to form a vacancy and therefore lower the equilibrium defect concentration (and carrier concentration). However, isoelectronic substitutions on the framework ($YbZn_{2-x}Cd_xSb_2$ and $YbZn_{2-x}Mn_xSb_2$) yield

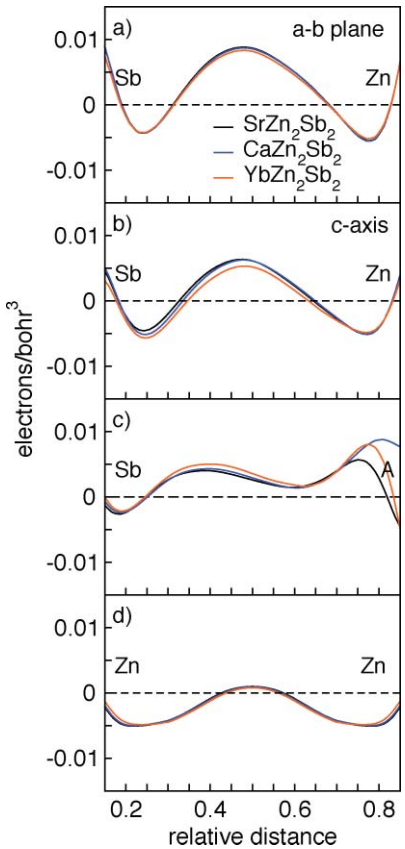

Fig. 9 To compliment Fig. 8, line scans between atoms in the unit cell showing charge accumulation and depletion for AZn$_2$Sb$_2$ (A = Sr, Ca, Yb). (a) Sb to Zn along the short bonds in the puckered 'a–b' plane, (b) Sb to Zn along the long c-axis bond (c) Sb to A-site cation, (d) Zn to Zn within the covalent slab.

noticeable effects on the carrier concentration but lack the large change in electronegativity. The energetics of vacancy formation are complex (including strain, entropy and competing phases); future work is required to determine the validity of this hypothesis.

From the resistivity and Hall coefficient (R_H) measurements, the Hall mobility ($\mu_H = R_H/\rho$) may be extracted (Fig. 3b). The solid line shown in Fig. 3b is a $T^{-3/2}$ fit of the lattice mobility (residual resistance included in the fit), which is roughly expected from acoustic phonon dominated mobility in a semiconductor. We use the quality of this fit to justify an acoustic phonon scattering model in the subsequent analysis.

A comparison of the mobility between different samples requires removal of the carrier concentration dependence (described below) to obtain the intrinsic mobility (μ_o). Fig. 4 shows curves for predicted mobility (300 K) as a function of carrier concentration based on experimental SrZn$_2$Sb$_2$ and YbZn$_2$Sb$_2$ transport properties. For A = Eu, Yb, a significantly higher mobility is obtained than for the A = Sr, Ca, and Ca–Yb solid solution compositions (μ_o = 245 and 112 cm^2 V^{-1} s^{-1}, for A = Yb and Sr, respectively). The room temperature mobility of YbCd$_2$Sb$_2$ from ref. 9 corresponds well to the SrZn$_2$Sb$_2$-based curve. The results from ref. 11 (not shown) are in between the lines in Fig. 4, possibly due to the presence of multiple impurity phases leading to a reduced mobility.

Carrier concentration dependence of the mobility in Fig. 4 was calculated using classic solutions to Boltzmann transport equations under the assumption that the hole mobility is limited by acoustic phonon scattering ($\lambda = 0$).[26] The reduced chemical potential (η) is determined from the Seebeck coefficient (Eq. 1, 2), and used to obtain the intrinsic mobility (Eq. 3). Here ζ is the reduced energy of holes, k is the Boltzmann constant, e is the electric charge, f_o is the Fermi distribution function, and Γ is the Gamma function. To convert from reduced chemical potential to carrier concentration, Eq. 4 is employed. In these calculations, the Hall coefficient is assumed to be unity, which is valid for high doping levels and/or low temperature.

$$\alpha = \frac{k}{e}\left(\frac{(2+\lambda)F_{1+\lambda}(\eta)}{(1+\lambda)F_{\lambda}(\eta)} - \eta\right) \quad (1)$$

$$F_r(\eta) = \int_0^{\infty} \zeta^r f_o(\eta) d\zeta \quad (2)$$

$$\mu_H = \frac{\mu_o \pi^{1/2} F_{\lambda}(\eta)}{2\Gamma(1+\lambda)F_{1/2}(\eta)} \quad (3)$$

$$n = \frac{4}{\sqrt{\pi}}\left(\frac{2\pi m^* kT}{h^2}\right)^{3/2} F_{1/2}(\eta) \quad (4)$$

With increasing temperature, decreasing carrier mobility (Fig. 3b) leads to increasing electrical resistivity (Fig. 5a). The decrease in the temperature dependence of the resistivity above 600 K is due to the thermal excitation of carriers. Also shown in Fig. 5a are previously reported resistivity data for AZn$_2$Sb$_2$, A = Ca, Yb, and Eu.[8,10]

Consistent with the electrical resistivity and Hall effect measurements, the Seebeck coefficient of SrZn$_2$Sb$_2$ (Fig. 5b) has the temperature dependence expected for a heavily doped semiconductor. In the near room temperature regime, a linear dependence with temperature is observed, and above 600 K the detrimental effects of minority carriers are observed. Similar behavior is observed for the AZn$_2$Sb$_2$, A = Ca, Yb, and Eu compounds, where larger carrier concentrations lead to lower Seebeck coefficients. A thermal band gap may be estimated experimentally from the peak Seebeck value and corresponding temperature ($E_g = 2e\alpha_{max}T_{max}$).[27] SrZn$_2Sb_2$ and CaZn$_2$Sb$_2$ are found to possess extremely similar bandgaps: 0.27 and 0.26 eV, respectively. The other compositions studied are too metallic to observe a thermal band gap within the temperature range investigated.

Fig. 6 shows the room temperature Seebeck coefficient *versus* carrier concentration across the AZn$_2$Sb$_2$ series (including the Ca$_x$Yb$_{1-x}$Zn$_2$Sb$_2$ solid solution). The theoretical curve utilizes a single, parabolic band assumption ($m^* = 0.56\ m_e$) to calculate the Seebeck coefficient from solutions to the Boltzmann transport equations (Eq. 1, carrier mobility limited by acoustic phonon scattering $\lambda = 0$). Eq. 4 is used to calculate the dependence of the Seebeck coefficient on carrier concentration. The remarkable agreement between the single band model and the rather diverse experimental data indicates these compounds have similar valence band edge features. This point will be discussed below in the context of band structure calculations.

In the absence of high temperature Hall effect measurements for all samples, the relationship between Seebeck coefficient and electrical conductivity provides insight into the nature of thermoelectric transport. Rowe and Min have shown, that for

a single parabolic band at the nondegenerate limit and constant relaxation time approximation, one expects $\Delta\alpha/\Delta\ln(\sigma) = -k/e$ (−86 μV/K).[28] Fig. 7 shows that two separate lines with this slope are required to capture the AZn_2Sb_2 behavior. We emphasize that these compounds have very similar m^* and Fig. 7 demonstrates the increase in conductivity for a given Seebeck coefficient for the rare-earth containing samples.

Electronic structure

To better understand the transport behavior across the AZn_2Sb_2 family, band structure calculations were performed to investigate the bonding and valence band edge features.

Bonding. Density functional calculations offer the possibility to extract the electron density, which can be post-processed in numerous ways to illustrate, both qualitatively and quantitatively, the reorganization of electron density caused by the formation of bonds. In this work we generate a procrystal composed of the superposition of free atom electron densities, which represents the electronic configuration in a non-bonded crystal. To visualize the electron density reorganization, we take the difference between the crystal and procrystal electron density. The accumulation of electron density in $SrZn_2Sb_2$ is represented by the isosurface in Fig. 8a and the depletion is shown in Fig. 8b. The corresponding line scans between atoms in the unit cell are shown in Fig. 9, where positive and negative values represent increases and decreases in electron density, respectively. To begin, we observe the significant electron accumulation along the Sb–Zn 'a–b' plane as three lobes around Sb, Fig. 8a. The line scan (Fig. 9a) reveals that this Sb–Zn bond is largely covalent with a bias towards the Sb, as expected from the electronegativity difference between these atoms. There is also electron accumulation between the longer, but similar c-axis Sb–Zn bond (see Table 2 for bond lengths). Again, the more electronegative Sb biases the electron distribution. Comparing Fig. 9a and b, the shorter bonds appear more electron-dense relative to the starting procrystal density.

Electron counting using the Zintl formalism would formally leave the A-site cation as 2+ with a lone pair extending into the cation monolayer from the Sb, similar to the electron accumulation seen in Fig. 8. The attraction between the lone pair and the cation monolayer, which is largely responsible for the puckering of the Zn–Sb slab, is clearly visible as electron accumulation in Fig. 8a, where lobes at Sr point towards Sb. Line scans show this bond to be fairly asymmetric and slightly larger for Yb than Sr or Ca (Fig. 9c). This difference can be rationalized by the increased electronegativity of Yb compared to Ca or Sr, which leads to less electron transfer to the anionic slab. Concurrent with the increased Sb–Yb bonding is a weakening of the Zn–Sb bonds, which is more dominant for the c-axis bond.

When covalent bonds form, atoms experience a local depletion of electron density as the orbitals rearrange to set up bonds. Indeed, all atoms in the unit cell, including anionic Sb, exhibit depletion near the core. Depletion around Zn is highly directional (three lobes in Fig. 8b) and appears as the dual of the electron accumulation around Sb. Fig. 9d provides additional visualization of the depletion around Zn. Due to the puckering of the Zn–Sb sheets, the Sr–Zn distance is quite large (~3.7 Å), and no bond is formed. As a consequence, there is electron depletion along Sr–Zn in favor of the electron accumulation along Sr–Sb.

Band structure. The projected densities of states (DOS) for AZn_2Sb_2 (A = Ca, Sr, Yb) are shown in Fig. 10. All compounds show an overlap of Zn s and Sb p states in the valence region (−5 eV) which indicates a significant degree of hybridization between these states. This hybridization supports the polyanionic $(Zn_2Sb_2)^{-2}$ zintl nature of these materials described by Burdett and Miller.[7]

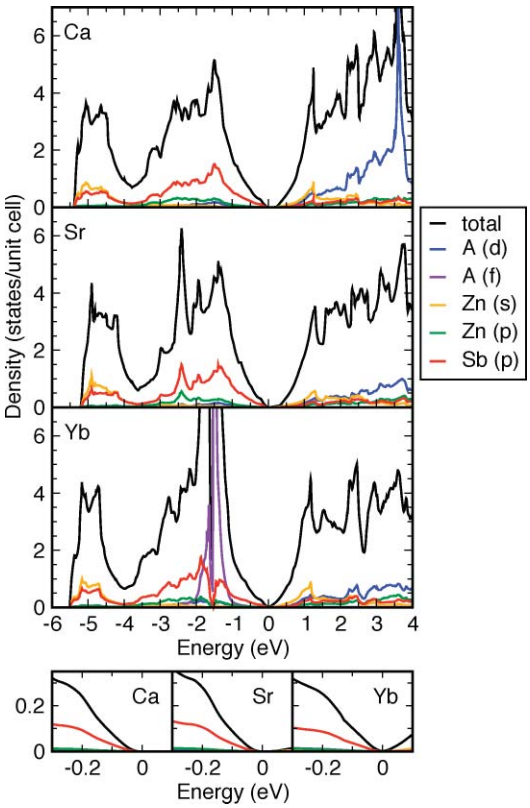

Fig. 10 The projected DOS for AZn_2Sb_2, A = Sr, Ca, Yb. The lower panels show the valence band edge within the range of the observed hole conduction.

Previous electronic structure calculations[29] predicted that $SrZn_2Sb_2$ does not possess a band gap. The observed thermal gap is 0.26 eV and this discrepancy likely originates from the common delocalization error inherited in the traditional exchange–correlation functionals of DFT. In this study we semi-empirically correct this by forcing a U = 10 eV for the Zn d states. It should, however, be emphasized that we did not chose this U based on an expected agreement with the experimental thermal gap. We choose it merely because this opens a small gap needed for the electron transport calculations. Also, extensive studies of the U as a function of the electron transport properties indicate that a U in this range is reasonable. For a more proper choice of U, experimental energy spectra are needed.

With a U of 5.3 eV utilized for Yb, the Yb f states peak approximately 1 eV below the band edge and extend up to the band edge (bottom panels of Fig. 10). For p-type conduction, we are primarily concerned with the valence band edge down to −0.2 eV. The addition of the Yb states at the valence band edge appears compensated by the decrease in Sb electron density, leading to a largely unaffected total density of states. The band structure at the valence band edge, shown in Fig. 11, consists of

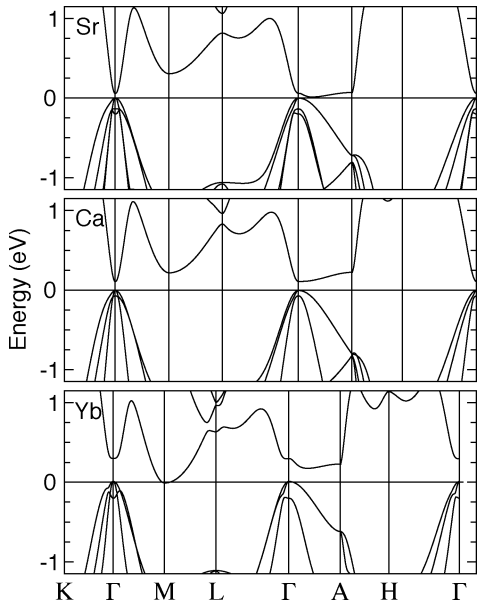

Fig. 11 Calculated band structure of the AZn_2Sb_2 (A = Sr, Ca, Yb) compounds for energies near the band gap.

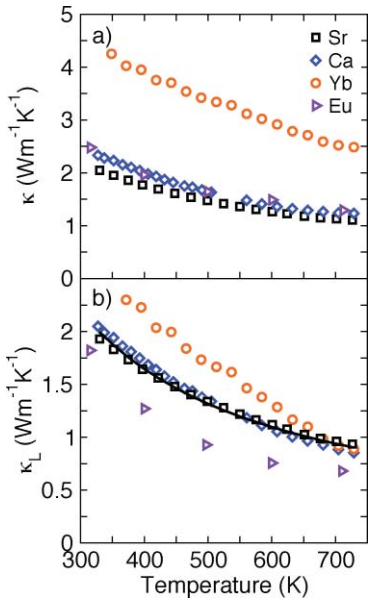

Fig. 12 (a) Thermal conductivity of AZn_2Sb_2 (A = Sr, Ca, Yb, Eu) varies greatly due to the difference in the electronic component of thermal conductivity (κ_e). (b) Subtracting κ_e reveals minimal difference in the lattice thermal conductivity between these compounds. The solid line shows a T^{-1} fit for $SrZn_2Sb_2$.

nested light and heavy bands which peak at close to the same energy. Deconvoluting the band crossings is nontrivial. The band differences between $SrZn_2Sb_2$ and $CaZn_2Sb_2$ is marginal, giving rise to essentially the same calculated first-principle Seebeck coefficient *versus* carrier density in Fig. 6. The qualitative agreement between the calculations and the experiments are acceptable.

The difference in mobility between the rare earth and Group II based compounds is surprising. Considering the classic definition of mobility ($\mu = e\tau/m^*$), the enhanced mobility in lanthanide compounds should be due to either an increased relaxation time or a decreased effective mass. Classical analysis of the Seebeck and Hall coefficients (described above), as well as density functional calculations, suggest the effective mass is very similar. The difference in mobility is most likely related to changes in τ arising from differences in microstructure and/or bonding features (transport anisotropy, bond covalency).

Thermal transport. Thermal conductivity (κ) is calculated from the product of the specific heat, density, and thermal diffusivity. In the absence of heat capacity measurements, the specific heat was estimated using the method of Dulong and Petit ($C_{DP} = 3k$ per atom). As heat is transmitted by both charge carriers and phonons, thermal conductivity is the sum of electronic (κ_e) and lattice (κ_L) components. Fig. 12 shows the total thermal conductivity of AZn_2Sb_2 (A = Sr, Ca, Yb, Eu) and the lattice thermal conductivity estimated by subtracting κ_e from κ_{total}. The Wiedemann–Franz relationship ($\kappa_e = L\sigma T$) estimates the electronic component from the Lorenz number (L) and the electrical conductivity. Here, we calculate L for each temperature by assuming single band behavior with the carrier mobility limited by acoustic phonon scattering, in which case the Lorenz number is given by Eq 5. For this calculation, η is obtained from $\alpha(T)$ using Eq. 1.

$$L = \left(\frac{k}{e}\right)^2 \frac{3F_0(\eta)F_2(\eta) - 4F_1(\eta)^2}{F_0(\eta)^2} \quad (5)$$

This estimation reveals that the AZn_2Sb_2 compounds have very similar κ_L values. Fig. 12b shows a T^{-1} fit to the κ_L of $SrZn_2Sb_2$, demonstrating the crystalline nature of the thermal conductivity of this compound.

Gascoin *et al*. looked at alloying $Ca_xYb_{1-x}Zn_2Sb_2$ to lower the lattice thermal conductivity.[10] Fig. 13 shows that this is quite successful, leading to a 50% reduction at 300 K. The dashed line is a fit assuming point defect scattering caused by mass fluctuation is dominant and follows the approach of Calloway.[30] The κ_L for disordered crystals can be described as a fraction of the lattice thermal conductivity without disorder ($\kappa_L{}^P$) *via* the disorder scaling parameter (u) in Eq 6.[31]

$$\frac{\kappa_L}{\kappa_L^P} = \frac{\tan^{-1}(u)}{u},\ u = \left(\frac{\pi^2\theta_D\Omega\kappa_L^P\Gamma_{calc}}{h\nu^2}\right)^{1/2} \quad (6)$$

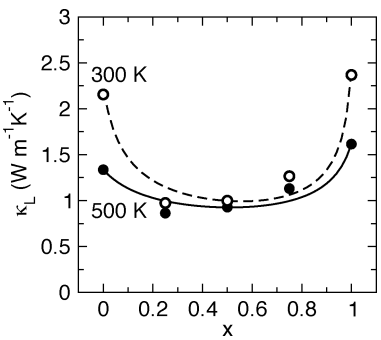

Fig. 13 Lattice thermal conductivity of the $Ca_xYb_{1-x}Zn_2Sb_2$[10] solid solution. The line shows the predicted reduction in κ_L from mass contrast scattering at 300 K and 500 K, derived from the end member compositions.

Determining u requires knowledge of the end member properties (average volume per atom Ω, average lattice sound velocity v)

and the calculated disorder scattering parameter (Γ_{calc}). We have previously reported v (2240 m/s) and θ_D (222 K).[32] In alloys, mass and strain field fluctuations both contribute to Γ_{calc}, however the Γ_{strain} should not contribute significantly as Ca^{2+} and Yb^{2+} ions are effectively identical in size (Table 2). The mass disorder scattering parameter is computed from the fractional occupancy, site degeneracy, and atomic masses as described in ref. 31. The quality of this fit confirms that point defects are the dominant phonon scattering source at this temperature. A similar reduction in lattice thermal conductivity upon alloying is also seen in $YbZn_{2-x}Cd_xSb_2$.[9] While point defect scattering lowers the lattice thermal conductivity, the effect on charge carrier mobility remains unclear. Both the AZn_2Sb_2 solid solutions investigated thus far have been between compounds with high ($YbZn_2Sb_2$) and low ($YbCd_2Sb_2$ and $CaZn_2Sb_2$) intrinsic mobilities. This question could be resolved by an investigation of the $Eu_{1-x}Yb_xZn_2Sb_2$ solid solution.

Thermoelectric efficiency

The thermoelectric figure of merit (zT) of AZn_2Sb_2 is shown in Fig. 14a, with a maximum value of 0.35 at 723 K for the previously uncharacterized $SrZn_2Sb_2$. From the experimental $SrZn_2Sb_2$ transport data, a theoretical zT curve can be calculated to predict performance as a function of carrier concentration (Fig. 14b, described below). An optimal carrier concentration of approximately 2×10^{19} cm^{-3} is obtained at 500 K, although at higher temperatures the effect of minority carriers must be considered. As expected from the differences in μ_o, the zT values of $YbZn_2Sb_2$ and $EuZn_2Sb_2$ do not fall on this curve. Increased μ_o does not significantly shift the optimal carrier concentration, and thus EuZ_2Sb_2 demonstrates a higher zT than YbZ_2Sb_2.[8,10] The reduction in κ_L from alloying likewise leads to zT values above the curve in Fig. 14b.

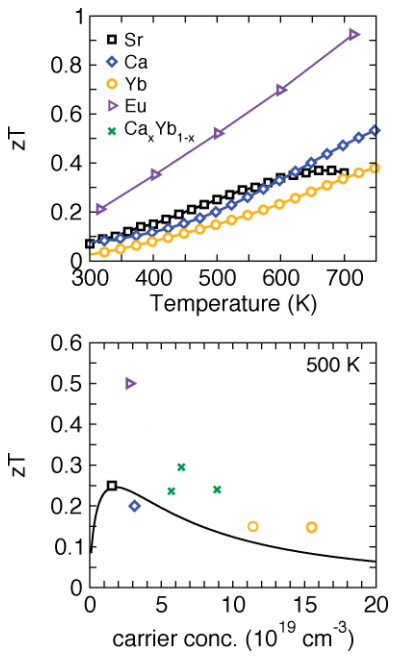

Fig. 14 (a) The thermoelectric figure of merit (zT) for AZn_2Sb_2 (A = Sr, Ca, Yb, Eu). (b) Predicted zT at 500 K from β parameter analysis of $SrZn_2Sb_2$. In the absence of high temperature carrier concentration data, room temperature values are used for $EuZn_2Sb_2$ and the $Ca_xYb_{1-x}Zn_2Sb_2$ solid solution.

The zT curve in Fig. 14b is calculated from Eq 7–9 assuming a single parabolic band and transport limited by acoustic phonon scattering ($\lambda = 0$). The fundamental material properties required for this theoretical calculation are obtained from Eq 1–5 using $SrZn_2Sb_2$ experimental data. The resulting relationship between calculated zT and η is translated to n *via* Eq 4.

$$zT = \frac{\alpha^2}{L + (\psi\beta)^{-1}} \tag{7}$$

$$\beta = \frac{\mu_o (m^*/m_e)^{3/2} T^{5/2}}{\kappa_L} \tag{8}$$

$$\psi = 2e\left(\frac{2\pi k m_e}{h^2}\right)^{3/2} \frac{F_\lambda(\eta)}{\Gamma[1+\lambda]} \tag{9}$$

Conclusions

The Zintl compounds AZn_2Sb_2 have the potential to be high efficiency thermoelectrics in the 600–800 K range due to their reasonably high mobility and low lattice thermal conductivity. Considering the effect of A-site species on electronic properties, the rare earth containing compounds exhibit larger mobility yet similar effective mass. This unusual behavior may be due to differences in τ arising from differences in microstructure and/or bonding. Single band analysis suggests the optimum carrier density is approximately 2×10^{19} cm^{-3}, consistent with the high zT reported for $EuZn_2Sb_2$. Future improvements to the thermoelectric efficiency of these materials will require approaches to control carrier concentration and reduce lattice thermal conductivity without a significant reduction to μ_o.

Acknowledgements

EST thanks the Beckman Foundation for support. We thank the DARPA-Nano Materials Program and NASA-JPL for funding and facilities. BCM gratefully thanks J. M. Rondinelli and K. T. Delaney for fruitful discussions regarding the band structure calculations as well as the NSF for support through a Career Award (DMR 0449354) to his research advisor Ram Seshadri at UCSB.

References

1 G. J. Snyder and E. S. Toberer, E. S., *Nat. Mater.*, 2008, **7**, 105.
2 S. M. Kauzlarich, S. R. Brown and G. J. Snyder, *Dalton Trans.*, 2007, **21**, 2099.
3 B. C. Sales, D. Mandrus and R. K. Williams, *Science*, 1996, **272**, 1325.
4 S. R. Brown, S. M. Kauzlarich, F. Gascoin and G. J. Snyder, G. J., *Chem. Mater.*, 2006, **18**, 1873.
5 E. S. Toberer, C. A. Cox, S. R. Brown, T. Ikeda, A. F. May, S. M. Kauzlarich and G. J. Snyder, *Adv. Funct. Mater.*, 2008, **18**, 2795.
6 A. Saramat, G. Svensson, A. E. C. Palmqvist, C. Stiewe, E. Mueller, D. Platzek, S. G. K. Williams, D. M. Rowe, J. D. Bryan and G. D. Stucky, *J. Appl. Phys.*, 2006, **99**, 023708.
7 J. K. Burdett and G. J. Miller, *Chem. Mater.*, 1990, **2**, 12.
8 H. Zhang, J.-T. Zhao, Y. Grin, X.-J. Wang, M.-B. Tang, Z.-Y. Man, H.-H. Chen and X.-X. Yang, *J. Chem. Phys.*, 2008, **129**, 164713.
9 X.-J. Wang, M.-B. Tang, H.-H. Chen, X.-X. Yang, J.-T. Zhao, U. Burkhardt and Y. Grin, *Appl. Phys. Lett.*, 2009, **94**, 092106.

10 F. Gascoin, S. Ottensmann, D. Stark, S. M. Haile and G. J. Snyder, *Adv. Funct. Mater.*, 2005, **15**, 1860.
11 C. Yu, T. J. Zhu, S. N. Zhang, X. B. Zhao, J. He, Z. Su and T. M. Tritt, *J. Appl. Phys.*, 2008, **104**, 013705.
12 X.-J. Wang, M.-B. Tang, J.-T. Zhao, H.-H. Chen and X.-X. Yang, *Appl. Phys. Lett.*, 2007, **90**, 232107.
13 A. Mewis, *Zeitschrift fuer Naturforschung*, 1978, **B 33**, 382.
14 J. A. McCormack and J. P. Fleurial, *Modern Perspectives on Thermoelectrics and Related Materials Symposium*, Materials Research Society, Anaheim, CA, 135 (1991).
15 J. Bérar and G. Baldinozzi, *IUCr-CPD Newsletter, IUCr-CPD*, (1998) 20, 3.
16 G. Kresse and J. Furthmüller, *Phys. Rev. B.*, 1996, **54**, 11169.
17 G. Kresse and D. Joubert, *Phys. Rev. B*, 1999, **59**, 1758.
18 P. E. Blöchl, *Phys. Rev. B*, 1994, **50**, 17953.
19 J. P. Perdew, K. Burke and M. Ernzerhof, *Phys. Rev. Lett.*, 1996, **77**, 3865.
20 P. E. Blöchl, O. Jepsen and O. K. Andersen, *Phys. Rev. B*, 1994, **49**, 16223.
21 A. I. Liechtenstein, V. I. Anisimov and J. Zaanen, *Phys. Rev. B.*, 1995, **52**, R5467.
22 P. M. Oppeneer, V. N. Antonov, A. N. Yaresko, A. Ya. Perlov and H. Eschrig, *Phys. Rev. Lett.*, 1997, **78**, 4079.
23 J. F. Herbst and J. W. Wilkins, in *Handbook of the Physics and Chemistry of Rare Earths*, edited by K. A. Gschneidner, L. Eyring, and S. Hüfner, (North-Holland, Amsterdam, 1987), Vol. 10, p. 321.
24 N. W. Ashcroft and N. D. Mermin, *Solid state Physics* (Brooks Cole, 1976).
25 I. Todorov, D. Y. Chung, L. Ye, A. J. Freeman and M. G. Kanatzidis, *Inorg. Chem.*, 2009, **48**, 47684776.
26 H. J. Goldsmid, *Applications of Thermoelectricity*, New York 1960 John Wiley and Sons.
27 H. J. Goldsmid and J. W. Sharp, *J. Elect. Mater.*, 1999, **28**, 869.
28 D. M. Rowe and G. Min, *J. Mater. Sci. Lett.*, 1995, **14**, 617.
29 G. K. H. Madsen, *J. Am. Chem. Soc.*, 2006, **128**, 12140.
30 J. Callaway and H. C. Von Baeyer, *Phys. Rev.*, 1960, **120**, 1149.
31 J. Yang, G. P. Meisner and L. Chen, *Appl. Phys. Lett.*, 2004, **85**, 1140.
32 A. F. May, E. S. Toberer and G. J. Snyder, *J. Appl. Phys.*, 2009, **106**, 013706.

